Progress report on OTF interferometric imaging using MeerKAT scanning observations

K. Rozgonyi[1], M. G. Santos[2,4], O. M. Smirnov[3,4] , J. J. Mohr[1,5], K. J. B. Grainge[6]

[1]University Observatory, Faculty of Physics, Ludwig-Maximilians-Universität, Munich, Germany, 81679
kristof.rozgonyi@physik.uni-muenchen.de
[2]Department of Physics and Astronomy, University of Western Cape, Cape Town, 7535, South Africa
[3]Department of Physics and Electronics, Rhodes University, PO Box 94, Grahamstown 6140, South Africa
[4]South African Radio Astronomy Observatory, Black River Park, 2 Fir Street, Observatory, Cape Town, 7925, South Africa
[5]Max Planck Institute for Extraterrestrial Physics, Giessenbachstrasse 2, Garching, Germany
[6]Jodrell Bank Centre for Astrophysics, Department of Physics and Astronomy, The University of Manchester, Manchester M13 9PL, UK

***Abstract*—'On-the-fly' (OTF) interferometric imaging enables fast survey speeds by removing the settle-and-slew overhead from traditional step and stare observations. Moreover, because HI intensity mapping requires scanning-mode observations, the OTF imaging enables commensal observing for intensity mapping and interferometric imaging, providing a dramatic improvement in data acquisition efficiency. An OTF observing mode would be highly beneficial for MeerKAT and the upcoming SKA; however, it is currently only available at the VLA. The aim of this report is to demonstrate that science-quality OTF interferometric imaging is possible with MeerKAT. By performing correlations during (standard) single-dish scanning mode observations where the delay center is set to a fixed point in the observer's reference frame the resulting scan data will support OTF interferometric imaging. We examine the errors inherent to such fixed delay center OTF observations, showing that for angular distances between the delay centre and the scan path of $\sim 6^\circ$ or less, the resulting phase smearing introduces flux errors at the percent level. The motion of the pointing centre on the sky during the visibility integration time introduces additional flux biases that can be corrected for by applying a 'smeared' primary beam correction. We develop a framework to transform the scan observations into OTF-format measurement sets and use them to produce OTF interferometric imaging snapshots that can then be combined into high quality mosaics. Although work is ongoing, we expect to deliver science-ready interferometric imaging data products from past and future intensity mapping scan datasets acquired with MeerKAT.**

I. Introduction

An OTF observing mode was developed for the VLA and has been used to carry out the VLASS survey [1]. With the dedicated OTF observing mode the correlator delay center tracks the scanning motion of the array primary beam (PB) response across the sky in a stepwise fashion. The main limiting data quality factor in comparison to traditional tracking observations is the smearing of the PB response for a given observing frequency ν and visibility integration time δt. This smearing is easily remedied, but it introduced only minor flux errors in in the VLASS survey [2] and was therefore left uncorrected.

With no dedicated OTF mode currently available on MeerKAT, scanning observations like those needed for intensity mapping can nevertheless be correlated and used after the fact for interferometric imaging. In this approach the correlator delay center tracks a fixed point in the array reference frame (e.g., point defined by fixed altitude and azimuthal angles on the sky). Ergo the delay centre has a time-dependent separation from the pointing centre of the antennae. In the case where the delay center is chosen to be the central point of an oscillatory scan, this separation can vary between $\pm$ few-to-tens of degrees, depending on the scanning strategy. This separation between the delay and pointing center amplifies the well-known smearing effects (bandwidth- and time-average smearing) considered in traditional tracked interferometric imaging.

In the following sections we describe the importance of such smearing errors, briefly discusses our imaging framework and present the first MeerKAT OTF interferometric images and associated mosaics where no correction for the smearing errors has been applied.

II. Errors specific to asynchronous OTF mode

Primary beam smearing

During the δt visibility integration time, the pointing centre moves relative to the phase-centre[1], which results in a smeared primary beam (PB) response. The smearing purely affects the PB shape, and thus, the measured flux density distribution of the image (i.e. it is an amplitude error). We can take the smearing into account by introducing an effective PB model, $B_{\nu,\mathrm{eff}}$. Although, the VLA only supports constant RA scans [2], with small Δs smearing distance, any arbitrary ($\Delta\alpha$, $\Delta\delta$) direction scans can be described with a linear smearing model around (α_0, δ_0) central RA, Dec coordinates. The general form for a smeared Gaussian PB model is given in eq. 1.

[1]The point on the sky which will form the origin for a map produced. As later discussed, we phase-rotated the observed visibilities from the delay centre to the pointing centroid for each δt visibility integration time.

$$B_{\nu,\mathrm{eff}}(\alpha_0,\delta_0,\Delta\alpha,\Delta\delta) = \frac{\sigma_\nu}{\Delta s}\sqrt{\frac{\pi}{2}}\exp\Big(-\Big[\alpha_0\frac{\Delta\delta}{\Delta s}+\delta_0\frac{\Delta\alpha}{\Delta s}\Big]^2/2\sigma_\nu^2\Big)\Big[\mathrm{erf}\Big(\frac{\alpha_0\frac{\Delta\alpha}{\Delta s}-\delta_0\frac{\Delta\delta}{\Delta s}+\frac{\Delta s}{2}}{\sigma_\nu\sqrt{2}}\Big)-\mathrm{erf}\Big(\frac{\alpha_0\frac{\Delta\alpha}{\Delta s}-\delta_0\frac{\Delta\delta}{\Delta s}-\frac{\Delta s}{2}}{\sigma_\nu\sqrt{2}}\Big)\Big] \quad (1)$$

$$\text{where} \quad \Delta s = \sqrt{\Delta\alpha^2+\Delta\delta^2}$$

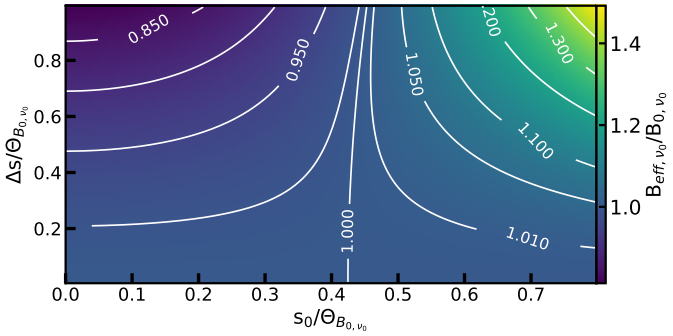

Fig. 1. OTFM smearing for MeerKAT at ν_0=1.7GHz. The smearing distance, Δs, is given in units of the reference PB FWHM, Θ_{B_0,ν_0}. s_0 denotes the distance from the PB centre in the direction of the smearing motion.

To estimate the effect of PB smearing, we followed [2] and computed the fractional beam change between the effective and conventional Gaussian PB model. Figure 1. shows the fractional beam change for different smearing values within the PB area. We computed both models at 1712 MHz (top of the L-band), where the smearing effect is the most severe for L-band MeerKAT observations. For the PB FWHM, we adopted a frequency scaling from [3], which gives a PB FWHM, Θ_{B,ν_0}=50′.98 at ν_0=1712MHz.

As shown, for Δs <0.4 $\Theta_{B_{0,\nu_0}}$, the fractional error is <5%. As such, for a few second integration time with relatively slow slewing speed (up to ∼10'/s in the observer's frame) the PB smearing error is negligible for MeerKAT L-band observations. Thus, the image flux density errors are likely to be dominated by other effects. Note that this effect is additive in linear mosaicking. Nonetheless, we could neglect the smearing effect for slow scanning speeds. For more details, see [4][2].

Bandwidth-. and time-average smearing

In the classical theory of synthesis imaging, the measured visibilities are not representing a single point in the (u,v) plane but an average measured over an area. For a single baseline of an East-West interferometer observing one of the poles, averaging in time is equivalent to averaging along the circular loci of the baseline, while averaging in frequency equals radial averaging. Averaging in both directions in the (u,v) plane is equivalent to angular smearing of sources in the image plane. The smearing is zero at the phase centre and increases with angular distance. Bandwidth- and time-average smearing are innate to synthesis imaging and are well-known since the early days of interferometry (see, e.g. [5]).

For traditional pointed observations, smearing is generally considered within the imaged area relative to the image centre (i.e. the phase centre). However, for asynchronous OTF observations, we need to consider these effects between the imaged area – centred at the pointing centre for maximal sensitivity – and the delay centre defined by the correlator. Hence, asynchronous OTF imaging inherently enhances these smearing errors which can be challenging to account for after the correlation process. Note that the smearing effect can be reduced by observing with finer spectral and/or time resolution or tracking the antennas' pointing centre during the correlation process. The latter results in OTF snapshot observations with *no* additional phase error on the observed visibilities compared to pointed observations.

We used a simple formalism of computing decoherence to estimate smearing effect(s) originating from averaging in the (u,v) plane. For $\Delta\phi$ (absolute) maximum phase difference between two plane waves, the coherence, C can be expressed as[3]:

$$C \simeq 1-\frac{\Delta\phi^2}{6} = 1-C_d \quad (2)$$

where C_d is the decoherence, representing the fractional phase uncertainty on the observed visibilities.

We could derive $\Delta\phi$ as a function of angular distance from the phase centre $\Delta\Theta$ for both bandwidth- and time-average smearing, using the simple smearing model described above.

Bandwidth smearing, or radial averaging in the (u,v) plane, $\Delta\phi_\nu$, at $\Delta\nu$ bandwidth and $\Delta\Theta$ separation can be expressed as:

$$\Delta\phi_\nu = \frac{1}{2}\frac{\Delta\nu}{\nu}\frac{b}{\lambda}\sin(\Delta\Theta) \quad (3)$$

where b is the baseline length, ν is the central observing frequency and λ is the observed wavelength. Note that, indeed, the smearing is *independent* from the observing frequency, only dependent on the bandwidth. Nonetheless we provide smearing int his form as it is expressed with the fractional bandwidth and the fractional baseline length.

Time-average smearing, or averaging along the baseline loci in the (u,v) plane, $\Delta\phi_t$, can be expressed with the Earth's rotation during the δt integration time in the following form:

$$\Delta\phi_t = \frac{1}{2}\delta t\sin(\Delta\Theta)\omega\frac{b}{\lambda} \quad (4)$$

[2]The MeerKLASS OTF memo series is not publicly available (yet), but can requested from the authors.

[3]For the derivation, we defined coherence as the ratio of the amplitudes of the correlated waves and the sum of the individual plane waves, with both the numerator and the denominator integrated over $-\Delta\phi$ and $+\Delta\phi$, i.e. considering the phase error introduced.

where ω is the Earth's angular rotation speed of $\sim 7.27\times10^{-5}$ rad/s.

For both smearing derivation, we took the sin() of $\Delta\Theta$, which is originating from the geometry of uncompensated path difference in a simple two-element interferometer, but is generally neglected due to the small angle of $\Delta\Theta$. Furthermore, the 1/2 term is introduced to account for the fact that the visibilites are averaged to the centroid in both time and frequency.

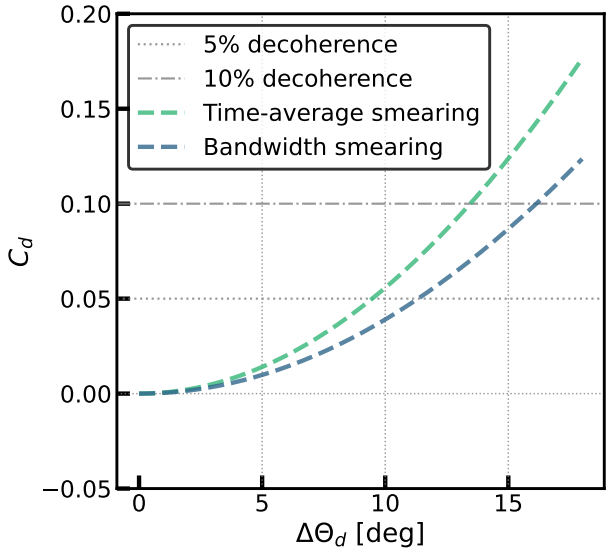

Fig. 2. Estimated decoherence due to bandwidth- and time-average smearing as a function of angular separation from the phase centre. See the main text for the observation parameters used.

To estimate the fractional smearing errors introduced in eq. 2., we computed the decoherence by substititing $\Delta\phi$ form eqs. 3. and 4., using δt=2s, ν=1.712GHz, $\Delta\nu$=209kHz and b=8km. Both the bandwidth and time-average smearing are shown in Figure 2. Note that this is the *maximum* smearing (on the longest baseline) for 4k channels L-band observations with 2s time-resolution. For a more detailed analysis, see [6].

We demonstrated that the inherent smearing effects are <5% for large angular separations. The estimated *maximum* phase error is ∼10% at 10 degrees away from the phase centre with the given observing parameters.

In conclusion, we can neglect both the PB smearing and the bandwidth and time-average smearing effects in imaging asynchronous OTF observations.

III. Data and imaging

Asynchronous OTF observations and the data used

We are currently working on the scanning data taken in 2021 as part of the open-time call MKT-20213 (PI: M. Santos, for the broader scientific details and observing strategy see e.g. [7], [8]). The observations were taken at L-band, 4k resolution with δt=2s integration time, 5'/s constant elevation scans, observing a primary calibrator (tracking part) and the target field (scanning part) for which, the correlator was switched on in the described 'asynchronous' fashion. In Fig 3. we show both the pointing and delay centers for an example segment from the scanning part of our observations. Three calibrator sources (PicA, 3C273 and J1934-6342) were used for the observations, from which only J1934-6342 can be used as an interferometric calibrator[4]. As such, we are only focusing on observations using J1934-6342, namely, we are developing our imaging pipeline using scheduling block 1630519596. Note that no secondary calibrator was observed, as the primary science goal for the observations was intensity mapping in auto-correlation mode.

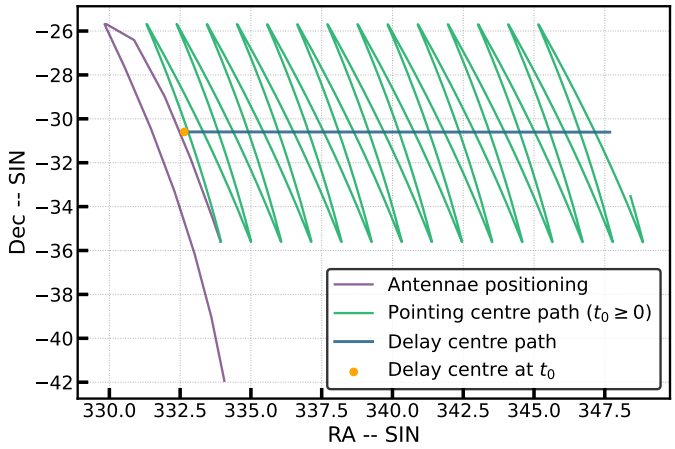

Fig. 3. Example 1h segment from the scanning part of our observations that is representative for our current asynchronous OTF observing setup. Note that the separation between the pointing and delay centers are <6°.

To image the cross-correlation data, we converted the MVF format data (provided by SARAO) to MS format using a custom version of `katdal`[5]. However, at this stage, the scans are not in OTF format as the observed delay centre is written to the MS instead of the pointing centre. Thus, we developed a pipeline[6], which applies a phase-rotation (using the `chgcentre`[7] tool from the WSClean package [9], and not `CASA` due to a small angle approximation used[8]) from the observed delay centre to the pointing centre, for every δt visibility integration time (i.e. an OTF snapshot or pointing). The pointing centre is determined from the pointing of a (reference) antenna using the auto-correlation data by matching the auto- (antenna pointing) and cross-correlation (visibility) data based on the time stamp. We found our data transformation pipeline scalable as we were able to convert hundreds of OTF pointings in a parallel fashion under ∼10 minutes on a personal computer.

Applying the phase rotation for each OTF pointing is the key to imaging asynchronous OTF observations since coherence

[4]In theory, with high-fidelity sky models both PicA and 3C273 could be used as calibrators, but this would require further observations to build the sky models.

[5]Katdal can be found on GitHub, and our custom version uses a simple hack to not ignore the scanning part in the `mvftoms.py` script.

[6]The pipeline can be found at GitHub.

[7]Description of the tool can be found at SourceForge

[8]The `CASA` tool `fixvis` uses a small-angle approximation and is deprecated, and while the task `fixvis` requires the configuration of the pointing tables, which we wanted to avoid to keep the code simple. For more details, see the `CASA` documentation

is preserved during the correlation process regardless of the antenna pointing direction relative to the delay centre. Ergo, the smearing errors discussed in the previous chapter are the *only* source of additional phase uncertainty introduced in comparison to pointed observation on the measured visibilities. Hence, after applying the correct phase rotation to the data, the resultant MS could be imaged using canonical imaging methods and software.

Imaging pipeline

Our proof-of-concept approach to OTF mosaic imaging is to image each 2s OTF pointing separately. We used `caracal` [10] to calibrate, image and mosaic the adjacent OTF snapshot images. We ran *only* an initial flagging on the scanning part of the data using `tricolour` [11], as most flagging methods run on the time-frequency space, and so, are not applicable to individual OTF snapshots. We applied the same initial flagging strategy for the calibrator field.

We followed a 'standard' calibration strategy to solve the delays, bandpass' and gains and calibrate for the absolute flux using the primary calibrator source. However, considering that no secondary calibrator was observed, we introduced two additional iteration in solving for the gains (phase and amplitude & phase) with 2s time resolution. We solved for the gains using ∼3.3. MHz (16 channels) resolution. We then transferred these solutions in imaging the OTF snapshots as an initial model for *in-field* self-calibration. We found that performing a single iteration of phase-only selfcal gain solving results in a stable gain solution. To account for the wide-bandwidth imaged, we used multi-frequency synthesis (MFS) imaging, currently with only two sub-bands[9], but we retain the 3.3 MHz spectral resolution when solving for the gains within each sub-band.

To create mosaic images, we are currently using the `montage` package [12] via `caracal`. We apply Gaussian PB correction for each MFS sub-band OTF snapshot image in mosaicking. However, we note that we should improve our image fidelity by accounting for higher resolution spectral variations during PB correction.

With our current pipeline, we are able to image sub-scans of 2minutes (61 OTF snapshots), and create mosaic images covering up to 15 adjacent OTF snapshot images[10] in an automated manner. Nonetheless, we are in parallel working on improving both the performance and precision of our pipeline and likely finalising the optimised parameters in the near future.

IV. Results up to date and future directions

We created OTF snapshots and mosaic images of a selected sub-scan up to date. An example patch from the sub-scan is shown in Fig. 4. The imaged OTF snapshots, show superb image quality with no (visual) trace of imaging artefacts. We measured the RMS levels close to the expected value (∼0.33 mJy/beam) on the individual snapshots. Furthermore, we performed source-finding on both single OTF snapshots and mosaics using `pybdsf` [13], and we found only sources with counterparts in other radio surveys such as NVSS [14]. While the source positions show excellent agreement with the NVSS values, the integrated flux of the sources shows some offset, which is likely originating from the low-accuracy of the PB correction used[11]. Nonetheless, our current results are highly encouraging by being close to science-quality, with no major systematic errors discovered so far. Ergo, our results are in good agreement with our prediction that the smearing effects are not significantly affecting the OTF snapshot images.

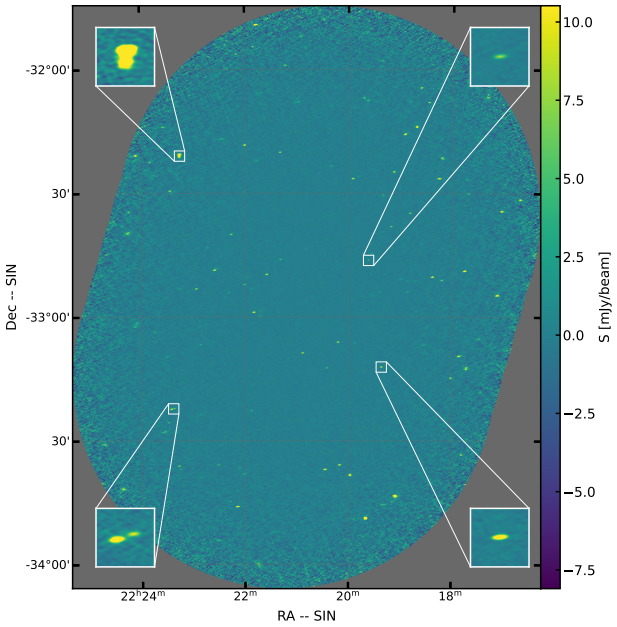

Fig. 4. OTF mosaic from 5 snapshots. The colour bar is given in units of mJy/beam, with the average synthesised beam of 19.9"×8.2" at -81.4deg. The colour bar is saturated at ±99.9% of the flux density distribution. Four example sources, with different morphology and brightness are highlighted.

We are currently iterating on our imaging pipeline parameters to improve on image fidelity. In addition, we are carrying out various analyses to measure the stability of our gain solutions, and to statistically measure the smearing effect by comparing peak fluxes to integrated fluxes as the function of distance from the phase centre over a whole scan, as only the former is expected to be affected by smearing for unresolved sources. These tests will feedback to the necessity and possible direction of future pipeline development.

We plan to image larger areas by scaling our pipeline deployment and to apply additional direction-dependent calibration on the combined OTF data to improve image fidelity. Furthermore, we would like to utilise in-field secondary calibrators, generate spectral and polarisation maps. However, this requires observations including secondary and polarisation calibrators, respectively.

[9]We are currently introducing higher MFS resolution to improve the restored flux density and the dynamic range of the image.

[10]With larger mosaic images, `montage` runs into memory issues (with 230 GB RAM allocated) and significantly slows down the mosaic process. We estimated that mosaicking a full sub-.scan would take >10 days, and so, we are currently looking to resolve this bottleneck.

[11]The analytics plots are currently updated frequently, but the most recent results can be requested from the authors.

ACKNOWLEDGMENTS

We thank for SARAO to enable the correlator during the scanning observations, and in particular for Ruby van Rooyen for providing us with the hack to convert scans from MVF to MS format. K. R. acknowledges support from the Bundesministerium für Bildung und Forschung (BMBF) award 05A20WM4.

REFERENCES

[1] M. Lacy *et al.*, "The Karl G. Jansky Very Large Array Sky Survey (VLASS). Science Case and Survey Design," , vol. 132, no. 1009, p. 035001, Mar. 2020.

[2] K. P. Mooley *et al.*, "The Caltech-NRAO Stripe 82 Survey (CNSS). II. On-the-fly Mosaicking Methodology," *ApJ*, vol. 870, no. 1, p. 25, Jan. 2019.

[3] T. Mauch *et al.*, "The 1.28 GHz MeerKAT DEEP2 Image," *ApJ*, vol. 888, no. 2, p. 61, Jan. 2020.

[4] K. Rozgonyi, "Thoughts on primary beam correction for MeerKLASS OTFM," LMU, Tech. Rep. MeerKLASS OTFM memo series no I., 2021.

[5] *Synthesis Imaging in Radio Astronomy II*, ser. Astronomical Society of the Pacific Conference Series, vol. 180, Jan. 1999.

[6] K. Rozgonyi, "Thoughts on visibility smearing in MeerKLASS asynchronous OTFM observations," LMU, Tech. Rep. MeerKLASS OTFM memo series no III., in preparation.

[7] M. G. Santos *et al.*, "MeerKLASS: MeerKAT Large Area Synoptic Survey," *arXiv e-prints*, p. arXiv:1709.06099, Sep. 2017.

[8] J. Wang *et al.*, "H I intensity mapping with MeerKAT: calibration pipeline for multidish autocorrelation observations," *MNRAS*, vol. 505, no. 3, pp. 3698–3721, Aug. 2021.

[9] A. R. Offringa *et al.*, "WSCLEAN: an implementation of a fast, generic wide-field imager for radio astronomy," , vol. 444, no. 1, pp. 606–619, Oct. 2014.

[10] G. I. G. Józsa *et al.*, "CARACal: Containerized Automated Radio Astronomy Calibration pipeline," Astrophysics Source Code Library, record ascl:2006.014, p. ascl:2006.014, Jun. 2020.

[11] B. V. Hugo *et al.*, "Tricolour: An Optimized SumThreshold Flagger for MeerKAT," in *Astronomical Society of the Pacific Conference Series*, ser. Astronomical Society of the Pacific Conference Series, J. E. Ruiz, F. Pierfedereci, and P. Teuben, Eds., vol. 532, Jul. 2022, p. 541.

[12] J. C. Jacob *et al.*, "Montage: An Astronomical Image Mosaicking Toolkit," Astrophysics Source Code Library, record ascl:1010.036, p. ascl:1010.036, Oct. 2010.

[13] N. Mohan and D. Rafferty, "PyBDSF: Python Blob Detection and Source Finder," Astrophysics Source Code Library, record ascl:1502.007, p. ascl:1502.007, Feb. 2015.

[14] J. J. Condon *et al.*, "The NRAO VLA Sky Survey," , vol. 115, no. 5, pp. 1693–1716, May 1998.